Doppler spectra of airborne ultrasound forward scattered by the rough surface of open channel turbulent water flows

Giulio Dolcetti, and Anton Krynkin

Citation: The Journal of the Acoustical Society of America **142**, 3122 (2017);
View online: https://doi.org/10.1121/1.5011183
View Table of Contents: http://asa.scitation.org/toc/jas/142/5
Published by the Acoustical Society of America

Doppler spectra of airborne ultrasound forward scattered by the rough surface of open channel turbulent water flows

Giulio Dolcetti[a] and Anton Krynkin
Department of Mechanical Engineering, The University of Sheffield, Mappin Street, Sheffield, S1 3JD, United Kingdom

(Received 24 June 2017; revised 2 October 2017; accepted 28 October 2017; published online 20 November 2017)

Experimental data are presented on the Doppler spectra of airborne ultrasound forward scattered by the rough dynamic surface of an open channel turbulent flow. The data are numerically interpreted based on a Kirchhoff approximation for a stationary random water surface roughness. The results show a clear link between the Doppler spectra and the characteristic spatial and temporal scales of the water surface. The decay of the Doppler spectra is proportional to the velocity of the flow near the surface. At higher Doppler frequencies the measurements show a less steep decrease of the Doppler spectra with the frequency compared to the numerical simulations. A semi-empirical equation for the spectrum of the surface elevation in open channel turbulent flows over a rough bed is provided. The results of this study suggest that the dynamic surface of open channel turbulent flows can be characterized remotely based on the Doppler spectra of forward scattered airborne ultrasound. The method does not require any equipment to be submerged in the flow and works remotely with a very high signal to noise ratio.

https://doi.org/10.1121/1.5011183

[DKW] Pages: 3122–3134

I. INTRODUCTION

The Doppler spectra of the signals of the airborne radar backscattered by the ocean water surface have been studied extensively in the past with the aim of characterizing the amplitude, period, and direction of the ocean waves.[1,2] Backscattered Doppler spectra are generally dominated by the Bragg scattering mechanism, which produces a stronger backscattering from the surface waves with the wavelength of approximately half the wavelength of the incident scattering wave.[3] In the microwave or airborne ultrasonic range of frequencies, the surface waves that are responsible for Bragg scattering are short capillary ripples, which are subject to modulations by longer waves[4,5] or by the flow current.[6] This complicates the interpretation of the measurements, especially in rivers[6,7] where the dynamics of short waves are still largely unknown.

Forward scattering occurs when the receiver is located in a near-specular direction with respect to the source. Forward scattering or so-called bistatic arrangements have been suggested as an alternative to backscattering, which enables the investigation of the spectrum of the longer and dominant waves in the ocean,[8,9] or the direct estimation of the wind and waves velocity.[10] If scattering is limited to the region of specular reflection, the Doppler spectra have a single maximum at the frequency of the incident signal. The width of the spectra relates to the relative roughness of the scattering surface,[11] and to the directivity pattern of the source.[12] Therefore, the behavior of the spectra can provide information about the statistics of the water surface. There are some advantages of the forward scattering arrangement with respect to the backscattering arrangement: (i) the dynamics of the larger surface waves that govern the behavior of the Doppler spectra are easier to measure, and more predictable; (ii) the signal-to-noise ratio is much higher than in backscattering; and (iii) the measurements can be carried out with a transducer with a broad directivity, allowing an investigation over a wide range of surface roughness scales.

In rivers, estimations of the mean flow velocity near the surface can also be obtained based on a delay-Doppler analysis applied to ultra high frequency radar in a bistatic configuration.[13,14] With this technique, the limited time delay resolution impedes the measurement of the longer waves that propagate parallel to the flow direction, which dominate the spectrum of the surface patterns,[15] ultimately eliminating the advantages of forward scattering over backscattering.[14] The scattering of ultrasound is easier to study and interpret compared to radio wave scattering due to the absence of polarization. The use of a narrowband signal in the forward scattering configuration eliminates the issue of time delay resolution, and the wide directivity allows the simultaneous observation of the surface behavior over a large area of the rough surface, including the region near the point of specular reflection where the signal-to-noise ratio is maximum.

In this work, the experimentally measured Doppler spectra of airborne narrowband ultrasound signals forward scattered by the water surface over a wide range of flow conditions are presented. The ultrasonic measurements were performed in a laboratory flume, where the statistics of the water surface were simultaneously characterized.[15] A linear random-phase model of the three-dimensional dynamic

[a]Electronic mail: g.dolcetti@sheffield.ac.uk

surface was developed based on the measured surface statistics, and implemented in a Monte Carlo simulation of the scattered acoustic field based on the Kirchhoff approximation. The linear random-phase model of the surface roughness employed in this work yields a Gaussian distribution of the surface elevation ζ.[16] The use of this model for the present study was justified by previous observations of Gaussian (at least at first-order) statistics of the water surface elevation in open channel turbulent flows,[17,18] over a similar range of flow conditions as the one described in this work. The comparison between the measured and modeled Doppler spectra allows a rigorous interpretation of the measurements, and demonstrates the link between the forward scattered acoustic field and the characteristic spatial and temporal scales of the water surface. These are linked to the hydraulic conditions of the turbulent flow by the parametric definition of the surface model, inspired by the experimental observations detailed in Ref. 15. The results of this study can pave the way for the development of a new range of remote measurement devices that are able to characterize the flow conditions remotely with a reliability superior to techniques based on backscattered Doppler.

The paper is organized in the following manner. The experimental acoustic setup and the hydraulic conditions of the investigated flows are reported in Sec. II. The numerical model is described in Sec. III. The numerical predictions of the Doppler spectra for different parameters of the water surface are described in Sec. IV. Experimental and numerical results are compared in Sec. V. Section VI summarizes the main results of the study. The fundamental equations that define the model of the dynamic water surface of an open channel turbulent flow over a rough bed are presented in the Appendix.

II. EXPERIMENTAL SETUP

A. Acoustic setup

For the experiments reported in this work, a 70 mm directional ultrasonic transducer (Pro-Wave ceramic type 043SR750, Pro-Wave Electronics Corporation, New Taipei City, Taiwan, R.O.C.) emitting ultrasound with the frequency of 43 kHz was employed. A schematic of the measurement setup is shown in Fig. 1. The transducer was installed in a 12.6 m long and 0.459 m wide rectangular laboratory flume, at the distance of 8 m from the flume inlet. The transducer faced toward the inlet, and was inclined downward toward the bottom of the flume by the angle $\psi = 30$ deg. The scattered acoustic field was recorded with a 1/4 in. Brüel and Kjær (Brüel and Kjær, Nærum, Denmark) 4939-A-011 microphone with type 2670 pre-amplifier. The microphone was located at the distance of 692.8 mm from the transducer, toward the flume inlet. A flow of water with homogeneous mean depth H and mean surface flow velocity U_0 was circulated in the flume. The flume bed was covered with three layers of plastic spheres with the diameter of 25.4 mm, arranged according to a hexagonal compact lattice. Details of the hydraulic setup and of the dynamic behavior of the water surface observed in the experimental conditions are described in Ref. 15. Both the transducer and the microphone were installed along the flume centerline. Their elevation above the mean water surface level

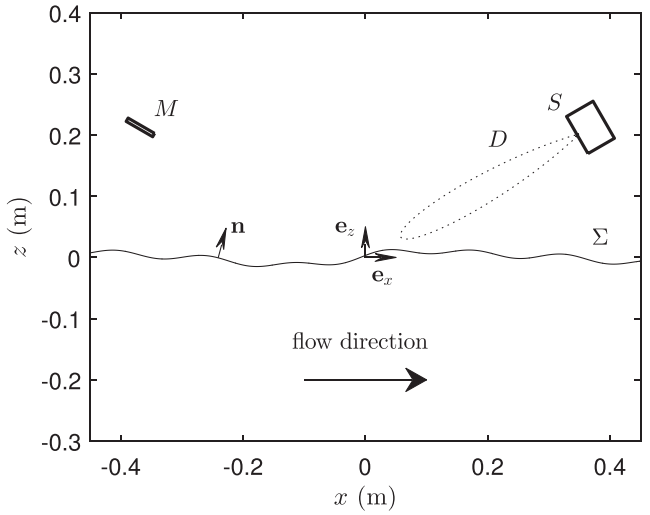

FIG. 1. A schematic of the measurement setup. The acoustic transducer indicated by the letter S emits ultrasound with the directivity patter D. This is scattered by the rough surface Σ with normal $\mathbf{n}$, and recorded by a microphone M.

was adjusted before each measurement and kept constant at 200 mm with an estimated uncertainty of 5 mm. The scattered acoustic field was recorded with the sampling frequency of 500 kHz. Fifty independent measurements of the acoustic field were performed in each of the flow conditions discussed in Sec. II B. Each measurement had the duration T equal to one second. The average of the Doppler spectrum across the 50 independent measurements was calculated according to Eq. (13).

The directivity pattern of the ultrasonic transducer at the frequency of 43 kHz was measured in an anechoic chamber. The details of these measurements have been described in Ref. 19. The directivity pattern of the same ultrasonic transducer used for this work was found to be approximated by the far-field directivity of a vibrating piston with radius $r_a = 20$ mm inserted in a rigid infinite baffle, i.e.,[20]

$$D(\theta) = 2\frac{J_1(\kappa r_a \sin(\theta))}{\kappa r_a \sin(\theta)}, \tag{1}$$

where J_1 is the Bessel function of the first kind, κ is the acoustic wavenumber $\kappa = \omega_a/c$, $c = 340$ m/s is the speed of sound, $\omega_a = 2\pi f_a$, and $f_a = 43$ kHz is the frequency of the scattered signal in air. θ is the angle with respect to the axis of the transducer. The response of the microphone was considered to be omnidirectional at the frequency used for this study.

Due to a relatively large distance between the transducer and the water surface, it was assumed that the scattering of ultrasound during the experiments occurred in the far-field. Therefore, the complex amplitude of the incident acoustic field at a generic coordinate $\mathbf{r}$ could be represented as

$$P_i(\mathbf{r},\mathbf{S}) = CD(\theta(\mathbf{r},\mathbf{S}))\frac{e^{i\kappa|\mathbf{r}-\mathbf{S}|}}{|\mathbf{r}-\mathbf{S}|}, \tag{2}$$

where $\mathbf{S}$ is the vector coordinate of the center of the transducer and C is a calibration factor related to the transducer sensitivity. The time-dependent incident acoustic field at the location $\mathbf{r}$ is given by

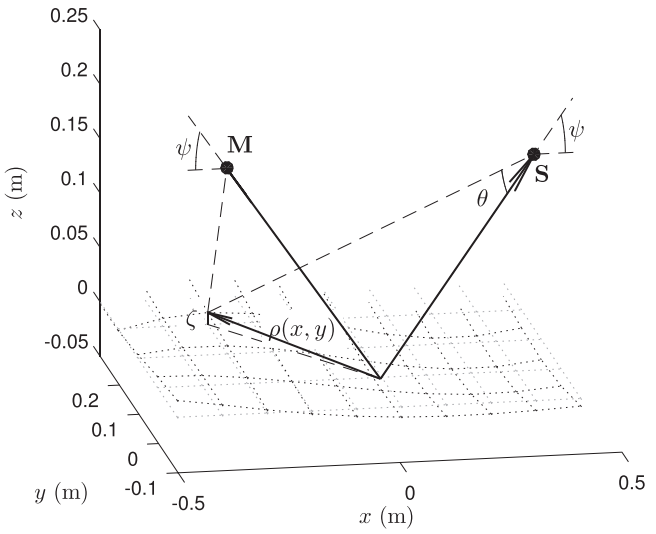

FIG. 2. Sketch of the geometry of the problem. The surface elevation ζ is defined with respect to the polar coordinate $\boldsymbol{\rho}$. The angle θ is measured from the axis of the transducer. The transducer and the receiver have the coordinates **S** and **M**, respectively, and their axes are inclined by the angle ψ with respect to the horizontal plane.

$$P(\mathbf{r},t) = P_i(\mathbf{r},\mathbf{S})e^{-i\omega_a t}, \tag{3}$$

where t is time and ω_a is the radian frequency of the input signal. At a fixed distance $|\mathbf{r}-\mathbf{S}|$ from the transducer, the maximum of the field amplitude is found along the main axis of the transducer, where $\theta(\mathbf{r},\mathbf{S})$ is equal to zero.

A schematic of the measurement setup with the definition of the system of reference is shown in Fig. 2. The x-y plane of the Cartesian coordinate system coincided with the flat water surface, which corresponded to the average elevation from the flume bed. The center of the coordinate system was located at the intersection of this plane with the axis of the transducer. The x axis was defined parallel to the flume centerline, oriented along the direction of the flow. The y-axis corresponded to the transverse direction. The elevation of the water surface in time and space was defined by the function $z=\zeta(x,y,t)$, where the z coordinate coincided with the normal to the average flat surface, pointing upward. For both the experiments and the numerical simulations reported in this work, the transducer and the receiver had the coordinates (in millimeters) of $\mathbf{S}=(346.4,0,200.0)$ and $\mathbf{M}=(-346.4,0,200.0)$, respectively.

B. Water surface parameters

The experiments were performed in a wide range of subcritical flow conditions, each one represented by different values of the homogeneous mean flow depth, H, and of the mean surface flow velocity, U_0. These quantities are reported in Table I for each measured flow condition, together with the corresponding Froude numbers and Reynolds numbers defined as $F = U_0/\sqrt{gH}$ and $\mathrm{Re} = U_0 H/\nu$, respectively, where g is the gravity constant and ν is the kinematic viscosity of water.

In the same range of flow conditions investigated in this study, Dolcetti *et al.*[15] demonstrated that the statistics of the water surface elevation are linked directly to the hydraulic flow conditions. The characteristic horizontal scale of the surface roughness is represented by the reciprocal of the wavenumber k_0, which is the wavenumber of the stationary waves. These waves are generated by the interaction of the flow with the rough static bed, and they propagate against the flow at a velocity equal to the mean surface velocity, so that they appear static to an external observer. In Ref. 15, the wavenumber k_0 and the dynamics of the water surface were determined based on a numerical procedure that allows taking into account the vertical variation of the time-averaged streamwise flow velocity.[21,22] This procedure becomes unstable when the velocity of propagation of the surface waves is smaller than the mean surface velocity, and when the waves propagate against the flow. Therefore, in this work the time-averaged streamwise flow velocity at each depth was approximated by its value near the surface, U_0. With this approximation, the wavenumber k_0 can be found as the solution of

$$k_0 U_0 = \sqrt{\left(g + \frac{\gamma}{\rho}k_0^2\right)k_0 \tanh(k_0 H)}, \tag{4}$$

where γ and ρ are the surface tension coefficient and the density of water, respectively. $k_0 U_0$ has the dimensions of a radian frequency, and it corresponds to the characteristic frequency of the surface fluctuations.[15]

TABLE I. Test flow conditions.

Flow condition	H (mm)	U_0 (m/s)	F (—)	Re (—)	σ (mm)	k_0 (rad/m)	$2k_0U_0$ (rad/s)
1	72.9	0.35	0.41	2.5×10^4	0.40	84.3	59.1
2	101.0	0.41	0.41	4.1×10^4	0.50	59.9	49.1
3	42.2	0.30	0.47	1.3×10^4	0.25	120.8	72.5
4	101.3	0.49	0.49	4.9×10^4	1.79	41.4	40.6
5	43.0	0.34	0.52	1.5×10^4	0.49	89.9	61.1
6	73.1	0.46	0.54	3.4×10^4	1.21	47.0	43.2
7	40.5	0.36	0.57	1.5×10^4	0.34	78.9	56.8
8	43.4	0.40	0.61	1.7×10^4	0.46	62.5	50.0
9	99.0	0.60	0.61	5.9×10^4	2.03	27.1	32.5
10	72.4	0.54	0.64	3.9×10^4	1.17	33.4	36.1
11	43.1	0.43	0.66	1.8×10^4	0.57	53.1	45.7
12	73.2	0.58	0.68	4.2×10^4	1.10	28.4	32.9

The dynamics of the water surface are described by the dispersion relation of gravity-capillary waves propagating over a flow with depth-wise constant time-averaged streamwise velocity,

$$\Omega(k,\beta) = kU_0|\cos(\beta)| + \text{sign}(\cos(\beta))\sqrt{\left(g+\frac{\gamma}{\rho}k^2\right)k\tanh(kH)}, \quad (5)$$

where k is the wavenumber modulus of the gravity-capillary waves on the free surface, and β is the angle between their direction of propagation and the x-direction. The first term on the right-hand side of Eq. (5) represents the advection by the flow, which is proportional to the mean surface velocity U_0.

The characteristic vertical scale of the surface fluctuations is represented by the standard deviation of the elevation function ζ, which is denoted by σ. A unique direct relationship between σ and the hydraulic conditions has not been identified yet. Therefore, the standard deviation was measured for each flow condition and at multiple locations using a set of conductance wave probes. These measurements are described with more detail in Ref. 15.

III. NUMERICAL MODEL

A. Acoustic model

The Kirchhoff approximation describes scattering from a smooth surface, where the condition

$$\chi = \kappa R_c \sin^3\psi \gg 1 \quad (6)$$

is satisfied. In Eq. (6), R_c is the curvature radius of the scattering surface and ψ is the angle of incidence of the acoustic waves determined by the inclination of the transducer (see Fig. 2). χ is called the Kirchhoff parameter. In this study, the Kirchhoff parameter was determined based on an equivalent curvature radius R_c, calculated from the reciprocal of the Gaussian curvature K_c, as

$$R_c = \sqrt{\frac{1}{K_c}}, \quad (7)$$

where the standard formula for the Gaussian curvature is

$$K_c = \left[\frac{\partial^2\zeta}{\partial x^2}\frac{\partial^2\zeta}{\partial y^2} - \left(\frac{\partial^2\zeta}{\partial x\partial y}\right)^2\right]\left[1+\left(\frac{\partial\zeta}{\partial x}\right)^2+\left(\frac{\partial\zeta}{\partial y}\right)^2\right]^{-2}. \quad (8)$$

Based on the Kirchoff approximation, the acoustic potential field generated by a transducer with coordinates $\mathbf{S}=(x_s,y_s,z_s)$, scattered by the rough surface Σ, and recorded at the location $\mathbf{M}=(x_m,y_m,z_m)$ is equal to[23]

$$P(\mathbf{M},t) = e^{-i\omega_a t}\int\!\!\int_\Sigma \mathbf{n}(\boldsymbol{\rho})\cdot\nabla[P_i(\boldsymbol{\rho},\mathbf{S})G_0(\mathbf{M},\boldsymbol{\rho})]\,d\boldsymbol{\rho}, \quad (9)$$

where the variable of integration $\boldsymbol{\rho}=(x,y,\zeta(x,y,t))$ is defined on the rough surface Σ with unit normal vector $\mathbf{n}$. $G_0(\mathbf{M},\boldsymbol{\rho})$ represents the free-field Green's function, defined as

$$G_0(\mathbf{M},\boldsymbol{\rho}) = -\frac{1}{4\pi}\frac{e^{i\kappa|\boldsymbol{\rho}-\mathbf{M}|}}{|\boldsymbol{\rho}-\mathbf{M}|}. \quad (10)$$

In practice, the integration of Eq. (9) can be performed with respect to $\boldsymbol{\rho}_0=(x,y)$ on the average flat surface Σ_0, after a change of variable,

$$\boldsymbol{\rho} = \boldsymbol{\rho}_0 + \zeta\mathbf{e}_z, \quad (11)$$

where $\mathbf{e}_z$ is the unit vector in the direction z, and

$$d\boldsymbol{\rho} = \sqrt{1+\left(\frac{\partial\zeta}{\partial x}\right)^2+\left(\frac{\partial\zeta}{\partial y}\right)^2}\,d\boldsymbol{\rho}_0. \quad (12)$$

In this work, the average Doppler power spectrum of the scattered acoustic field was defined as[24]

$$S(\omega) = \frac{1}{T}\left\langle\left|\int_0^T P(\mathbf{M},t)e^{i(\omega+\omega_a)t}\,dt\right|^2\right\rangle, \quad (13)$$

where T was the total duration of one measurement, and the angular brackets represent averaging over a number of random realizations, or independent measurements. The definition of Eq. (13) was applied to both the experimentally measured scattered field and to its synthetic realizations obtained for random realizations of the surface ζ, based on the numerical integration of Eq. (9).

For the numerical model, the integrand of Eq. (9) was calculated on a rectangular two-dimensional grid with a grid spacing of Δr. The grid had the dimensions L_x and L_y in the x- and y-directions, respectively. Random realizations of the surface elevation in time were generated based on the procedure described in Sec. III B. The acoustic field was calculated independently for each realization at a discrete set of time intervals, according to a frozen-surface approximation.[24] The time step used for the analysis was defined as Δt. The factor $\exp(-i\omega_a t)$ was not considered during the calculation of the instantaneous field with Eq. (9) since it cancels out based on the definition of the Doppler spectrum in Eq. (13). This allowed increasing the time step above the limit imposed by the Nyquist criterion based on ω_a.

B. Surface model

According to the linear random-phase surface model implemented for this study, one realization of the surface elevation at the time t can be described by the cosine series[16]

$$\zeta(x,y,t) = \sum_p\sum_q \xi_{pq}a_{pq}\cos\left[\mathbf{k}_{pq}\cdot\boldsymbol{\rho}_0 - \Omega(\mathbf{k}_{pq})t + \Phi_{pq}\right], \quad (14)$$

where $\mathbf{k}_{pq} = k_p[\cos(\beta_q)\mathbf{e}_x + \sin(\beta_q)\mathbf{e}_y]$ is a wavenumber vector defined on the discrete grid $k_p = p\Delta k$, $p=0,1,\ldots$, and $\beta_q = q\Delta\beta$, $q=0,1,\ldots$. ξ_{pq} and Φ_{pq} are real random variables, and a_{pq} are the coefficients of the series. For a linear random-phase model, ξ_{pq} is normally distributed, and Φ_{pq} is uniformly distributed in the interval $(-\pi,\pi]$.[16] The evolution

of the surface in time is governed by a dispersion relation $\Omega(\mathbf{k}_{pq})$, such as the one presented in Eq. (5). The coefficients a_{pq} are obtained from the directional spectrum of the surface elevation $\Psi(k,\beta)$ by means of

$$\frac{a_{pq}^2}{2} = \int_{\Delta k_p}\int_{\Delta\beta_q} \Psi(k,\beta) k\, dk\, d\beta, \tag{15}$$

where $\Delta k_p = (k_p - \Delta k/2, k_p + \Delta k/2)$ and $\Delta\beta_q = (\beta_q - \Delta\beta/2, \beta_q + \Delta\beta/2)$ are intervals with size Δk and $\Delta\beta$ centered about k_p and β_q, respectively. In the study of water surface waves, the directional spectrum $\Psi(k,\beta)$ is often factorized as (e.g., Ref. 25)

$$\Psi(k,\beta) = \hat{\Psi}(k)\mathcal{D}(k,\beta) \tag{16}$$

in order to isolate the dependence on the direction of propagation β. The function $\mathcal{D}(k,\beta)$ is called the directional distribution of the surface waves, and it is, in general, a function of the wavenumber.

The generation of random realizations of the surface elevation requires the knowledge of the two factors of the surface directional power spectrum, $\hat{\Psi}(k)$ and $\mathcal{D}(k,\beta)$, and the dispersion relation $\Omega(k,\beta) = \Omega(\mathbf{k})$ given by Eq. (5). A general form of the surface directional spectrum has not been determined yet for the waves that propagate over a turbulent open channel flow. This spectrum cannot be inferred from the measurement of the surface frequency spectrum, especially when the flow mean surface velocity is of similar order of magnitude of the phase and group velocities of gravity-capillary waves.[26] For waves propagating in open channel flows where turbulence is generated by active or passive grids, Savelsberg and van de Water[27] measured a power-function spectrum with the form $\hat{\Psi}(k) \propto k^{-\alpha}$, and with the exponent $\alpha \approx 8$. Power-function spectra of the surface elevation have been predicted also theoretically based on the rapid distortion theory for the waves generated by turbulence in a vertically sheared flow.[28] In a range of flow conditions similar to the one investigated in this study, Horoshenkov *et al.*[17] suggested a Gaussian quasi-harmonic behavior of the spatial correlation function of the surface elevation, which indicates a Gaussian shape of the spectrum. This type of spectrum was found to largely underestimate the surface slopes when compared to measurements in a real river.[29]

Very few measurements of the directional distribution $\mathcal{D}(k,\beta)$ of the waves over turbulent flows have been presented. By comparing the spatial correlation of the surface elevation measured along the streamwise and the transverse directions, Savelsberg and van de Water[27] observed that the anisotropy of the surface spectrum was related to the eventual anisotropy of the turbulent flow in the case of grid-generated turbulence. Dolcetti *et al.*[15] observed a strong link between the period of the fluctuations of the spatial correlations and the wavelength of the stationary waves produced by the bed roughness, and measured spatial correlation functions that were only weakly dependent on the spatial direction. The apparent isotropy of the correlation measured in Ref. 15 was explained in terms of the predominance of waves with the same wavenumber k_0 that propagated in all directions. Teixeira and Belcher[28] presented theoretical predictions of the directional distribution of the waves generated by resonance with turbulence in a vertically sheared flow. These authors suggested a dependence similar to $\cos^2(\beta - \pi)$ (in the notation used for this study), with a slight broadening and the appearance of bimodal distributions at low wavenumbers. The observation of the $\cos^2$ distribution was limited to the waves that propagated against the flow and were able to resonate with it, while the growth of waves that propagate downstream with $|\beta| < \pi/2$ was not predicted by the theory presented in Ref. 28.

In this work, the power-function spectrum $\hat{\Psi}(k) \propto k^{-\alpha}$ observed in Ref. 27 was adopted since its significance for water waves over turbulent flows is well established.[28] The longest waves observed in Ref. 15 had the wavenumber modulus equal to k_0. Therefore, k_0 was chosen as the lower cutoff of the spectrum for this study. The numerical results presented in Sec. IV were obtained with two different values of α, namely, $\alpha = 5$ and $\alpha = 7$. These values are representative of the range of α that provided a better fit with the measured Doppler spectra also reported in Sec. IV, across the measured range of flow conditions. Values of the spectrum slope smaller than $\alpha = 5$ were found causing a decrease of the Kirchhoff parameter below the range where the Kirchhoff approximation is believed to be accurate due to the increased effects of short waves with larger curvature. Therefore, simulations with α smaller than 5 are not discussed in this study.

The experimental conditions investigated in this study were similar to those measured in Ref. 15 where the surface waves were suggested to be generated mainly by the interaction with the rough bed, and waves that propagated downstream were clearly identified, although with an amplitude smaller than that of the upstream-propagating waves. The $\cos^2$ distribution suggested in Ref. 28 is not able to represent both downstream- and upstream-propagating waves correctly. Therefore, in this study the function $\mathcal{D}(k,\beta)$ was described by means of two standard directional distributions, which have had applications in oceanography: the so-called Poisson distribution and the sech^2 distribution.[25] These are defined by Eqs. (A1) and (A2) in the Appendix. Dolcetti *et al.*[15] found that most short waves with the wavenumber modulus larger than k_0 were propagating either along or against the mean flow direction x, but always parallel to it. The waves with the wavenumber modulus equal to k_0, instead, were found to propagate in all directions. The power spectrum of these waves had a maximum for the waves that propagated against the flow direction, with $\beta = \pi$, while it had a minimum for the waves that propagated downstream, with $\beta = 0$. The ratio of the power spectra for the waves propagating in the two opposite directions, $\Psi(k_0,\pi)/\Psi(k_0,0)$, was found to be between 10 and 10^2 in Ref. 15. Both directional distributions used for this study depend on a single parameter, b. This parameter defines the value of the ratio

$$\mathcal{L} = \tilde{\mathcal{D}}(\pi)/\tilde{\mathcal{D}}(0), \tag{17}$$

where $\tilde{\mathcal{D}}(\beta) = \mathcal{D}(k_0,\beta)$ is the directional distribution of the waves with wavenumber $k = k_0$. For these waves, the value

$\mathcal{L} = 10^{1.5}$ was chosen, in accordance with the observations in Ref. 15.

In order to represent the different behavior of the various types of waves observed in Ref. 15 (namely, waves with wavenumber modulus $k = k_0$ propagating in all directions, and waves with wavenumber modulus $k \geq k_0$ propagating only parallel to the x-direction, with $\beta = 0$ or $\beta = \pi$), a set of delta functions were introduced in the general definition of the directional spectrum as follows:

$$\Psi(k,\beta) = \tilde{\Psi}(k)\tilde{\mathcal{D}}(\beta) \times \left\{ \delta(k-k_0) + \frac{H(k-k_0)}{k}[\delta(\beta)+\delta(\beta-\pi)] \right\}. \quad (18)$$

In Eq. (18), H is a Heaviside step function, δ is a delta function, and

$$\tilde{\Psi}(k) = \Psi_0 \left(\frac{k}{k_0}\right)^{-\alpha}. \quad (19)$$

The delta functions in Eq. (18) select the specific types of waves observed in Ref. 15 and impose either their wavenumber modulus or their direction of propagation deterministically. The term $\delta(k - k_0)$ in Eq. (18) identifies the waves with the constant wavenumber modulus k_0, which propagate radially, with an amplitude that is governed by the directional distribution $\tilde{\mathcal{D}}(\beta)$. Replacing $k = k_0$ in Eq. (5), and letting β vary between $-\pi$ and π with the definition of k_0 provided by Eq. (4), one finds that the frequency of these waves varies between 0 (when $\beta = \pi$) and $2k_0U_0$ (when $\beta = 0$). The terms with $\delta(\beta)$ and $\delta(\beta - \pi)$ in Eq. (18) represent waves that propagate downstream and upstream, respectively, parallel to the direction of the flow. The spectrum of these waves decays like $\propto k^{-\alpha}$ according to Eq. (19), and their wavenumber modulus is $k \geq k_0$ as a result of the Heaviside step function. The waves that propagate downstream with $\beta = 0$ have the frequency larger than $2k_0U_0$, while the waves that propagate upstream with $\beta = \pi$ can have any frequency larger than 0. As a result of employing the same factor $\tilde{\mathcal{D}}(\beta)$ across the whole range of wavenumbers in Eq. (18), the same ratio $\mathcal{L} = 10^{1.5}$ between the amplitude of the upstream-propagating and downstream-propagating waves was effectively extrapolated to the shorter waves with $k > k_0$.

The synthetic surface realizations that were implemented in the acoustic model described in Sec. III A were determined based on Eq. (14), where the coefficients a_{pq} were calculated based on the spectrum defined in Eq. (18). The specific shape of this spectrum allowed the separation of the terms of the cosine series that pertain to the different types of waves, so that three distinct sets of summations over a single index could replace the double summation in Eq. (14). The details of these calculations are reported in the Appendix.

Although the spectrum described by Eq. (18) may not apply, in general, to the waves at the free surface of turbulent flows, it is believed that its simple standard formulation would allow an easy future validation or eventual improvement of the results presented in this study. Meanwhile, the choice to use two different directional distributions and two different values of the spectrum exponent α enable the observation of the effects of the shape of the surface spectrum on the acoustic Doppler spectra.

C. Numerical computation

Synthetic surface realizations were generated according to Eq. (14) with formulae (A3)–(A8), based on the values of k_0 obtained from Eq. (4), and based on the measured standard deviation of the surface elevation, σ, reported in Table I. In these realizations, ζ was evaluated on the same spatial and temporal grid employed in the acoustic model. This grid had the dimensions $L_x = 2$ m, $L_y = 0.5$ m, and the grid spacing $\Delta r = \lambda_a/10$, where λ_a was the acoustic wavelength at the frequency of 43 kHz, equal to 7.9 mm. The grid spacing on the surface was smaller than the value recommended for boundary element methods calculations,[30] $\lambda_a/5$, and it was sufficient to reach good convergence in the acoustic calculations. The coefficients of Eq. (A3) were calculated using $\Delta\beta = 2\pi/251$ rad, $q = 1,2,\ldots,2\pi/\Delta\beta$ and $\Delta k = 2\pi/L_x$, $p = k_0/\Delta k, \ldots, k_N/\Delta k$, so that only the waves with the wavenumber $k_0 \leq k_p \leq k_N$ were modeled, where $k_N = 2\pi/0.005$ rad/m, corresponding to a wavelength of 5 mm. The value of $\Delta\beta$ was chosen in order to ensure that $k_0\Delta\beta < \Delta k$ for each flow condition. The time length of each realization was $T = 1$ s, similar to that used in the experiments, and the time step used in the simulation, Δt, was equal to 0.001 s.

The Kirchhoff parameter χ was calculated at each realization based on Eq. (6), with the characteristic angle of incidence ψ equal to 30 deg, and with the radius of curvature R_c given by Eq. (7). R_c varies in space and time with the gradients of the surface elevation. In order to check the validity of the Kirchhoff approximation, the minimum of R_c was calculated in space for each surface realization. The calculation was limited to the instantaneous surface realizations at the instant $t = 0$, in light of the ergodicity of the process. An absolute minimum was then identified across all realizations, and replaced into Eq. (6) to estimate the minimum expected value of the Kirchhoff parameter χ. Across all simulations presented in this work, this minimum was found to be equal to 6.5, calculated for flow condition 3 and $\alpha = 5$. This value is believed to be sufficient to assume the validity of the Kirchhoff approximation in the range of conditions investigated in this study.

The validity of the surface model was tested by comparing the average frequency power spectra and zero time-lag spatial correlation functions of the synthetic surface with those measured by means of arrays of conductance wave probes in the way described in Ref. 15. The average frequency spectra of the measured and synthetic surfaces are shown in Fig. 3(a), while the corresponding correlation functions are shown in Fig. 3(b), as determined for flow condition 6. Both the measured and modeled frequency spectra shown in Fig. 3(a) have a maximum at zero frequency, which indicates the presence of stationary waves on the surface. The spectra are broad, and initially they decay slowly with the frequency. The numerical model based on the

spectrum of Eq. (18) overestimates the amplitude of the frequency spectrum of the surface fluctuations at the frequency of ∼43 rad/s. This frequency is indicated by a red line in Fig. 3(a), and it corresponds to the value of $2k_0U_0$ for condition 6. Such a frequency is also the maximum frequency of the waves with wavenumber $k = k_0$ according to Eq. (5). At higher frequencies, the frequency spectrum of the synthetic surface shown in Fig. 3(a) decays more rapidly due to the $k^{-\alpha}$ decay of the spectrum of short downstream propagating waves. This is consistent with the behavior of the experimental spectrum shown in Fig. 3(a), and with the observations reported in Ref. 15. In the higher-frequency region of the spectrum of Fig. 3(a), the measurements are approximated more closely by the model with $\alpha = 5$ than the one with $\alpha = 7$.

The apparent peak of the frequency spectrum of the synthetic surface at the frequency of $2k_0U_0$ was caused by a zero of the gradient with respect to β of the dispersion relation of the waves with wavenumber k_0. This gradient is defined as

$$\frac{\partial \Omega(k_0, \beta)}{\partial \beta} = -k_0 U_0 \sin(\beta), \tag{20}$$

and it becomes zero when $\beta = 0$ or $\beta = \pi$. Defining the surface frequency spectrum as[26]

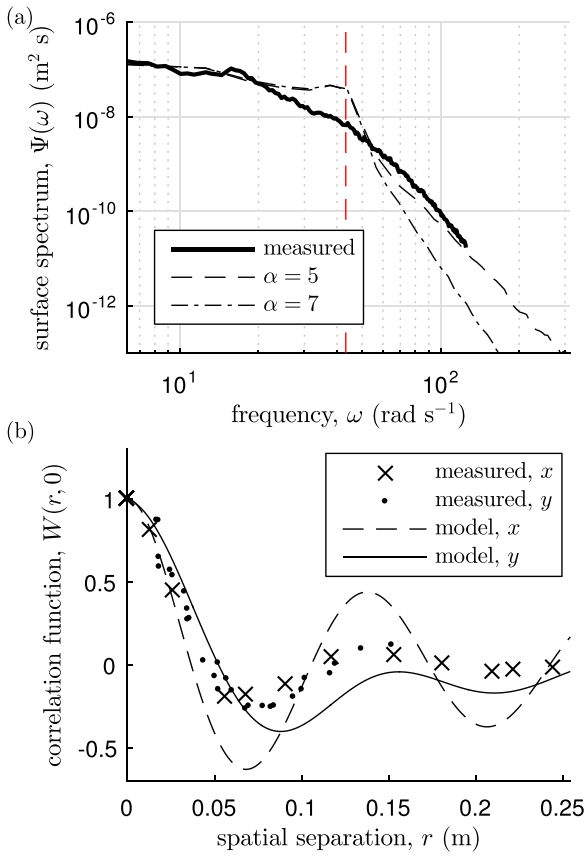

FIG. 3. (Color online) Examples of (a) the frequency spectrum and (b) the zero time-lag correlation function of the surface elevation, for condition 6. (Thick line and symbols) Measurements, (thin lines) modeled. The modeled results in (b) were obtained with $\alpha = 5$.

$$E(\omega) = \int_0^\infty \int_0^{2\pi} \Psi(k, \beta)\delta(\omega - \Omega(k, \beta))k\, dk\, d\beta, \tag{21}$$

and expressing the delta function as a function of β, the gradient of Ω appears at the denominator of the integrand in Eq. (21). Substituting in Eq. (21) the spectrum of Eq. (18), one finds an integrable singularity of the integrand at $\omega = \Omega(k_0,0) = 2k_0U_0$. This singularity would disappear if the stochastic variation of the flow mean surface velocity U_0 or of the wavenumber k were considered, since in this case the delta functions in Eqs. (18) and (21) would be replaced by smooth probability functions. These variations are not considered in the simplified surface model used for this work. As a result, the frequency spectrum of the synthetic surface realizations does not follow the smooth decay of the measured spectrum.

The zero-time lag spatial correlation functions are shown in Fig. 3(b), where they are plotted against the spatial separation between the measurement locations on the surface. The correlation functions of the measured and synthetic surfaces both show a quasiperiodic fluctuation with the period of approximately $2\pi/k_0 = 0.13$ m in both directions x and y, respectively. The relation between the period of the spatial correlation function and the wavenumber k_0 was observed in Ref. 15. The correlation function of the synthetic surface showed in Fig. 3(b) has a larger amplitude of the fluctuations compared to the measurements, especially along the x-direction. Similarly to the peak of the frequency spectrum at the frequency of $2k_0U_0$, the larger fluctuations of the correlation function can be explained in terms of a singularity of the kernel of the streamwise wavenumber spectrum associated with the deterministic directional spectrum used for this study. It is suggested that replacing the delta functions used in Eq. (18) with realistic probability density functions could provide a more accurate comparison with the measurements.

Regardless of these discrepancies, which are shown in Sec. V A to affect the predictions of the acoustic Doppler spectra only at the Doppler frequency of approximately $2k_0U_0$, Figs. 3(a) and 3(b) show that the proposed surface model was able to represent the behavior of the water surface measured during the experiments at least qualitatively for flow condition 6. The experimental results reported in Ref. 15 showed a similar behavior of the frequency spectra and the correlation function of the surface elevation, across a similar range of flow conditions to that investigated in this study. It should be noted that for flow condition 3, which is discussed more extensively in Sec. IV, the characteristic scales of the free surface roughness were found to be close to the resolution of the measurements reported in Ref. 15. As a result, the fluctuations of the measured correlation function were not observed for this condition, and the behavior of the frequency spectrum of the elevation at high frequency was not discussed in Ref. 15. Therefore, in Fig. 3 it was preferred to show the comparison between the statistics of the measured and the modeled surface for condition 6. This condition had an intermediate Froude number; therefore, it is believed to be representative of the typical behavior of the

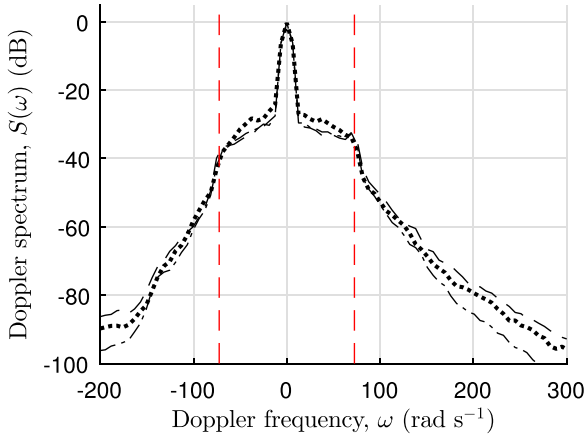

FIG. 4. (Color online) Examples of the simulated Doppler spectra for flow condition 3 ($k_0 = 120.8$ rad/m, $\sigma = 0.25$ mm, $U_0 = 0.30$ m/s). (Dashed) $\alpha = 5$, Poisson distribution, (dashed-dotted) $\alpha = 7$, Poisson distribution, (dotted) $\alpha = 5$, sech^2 distribution. The red lines indicate the characteristic frequencies $\pm 2k_0U_0$.

water surface. The significance of the proposed surface model over a wider range of flow conditions is demonstrated by the comparison between the measured and modeled acoustic Doppler spectra in Sec. V A.

IV. NUMERICAL RESULTS

In this section, the effects of the different parameters of the dynamic water surface model [namely, the horizontal scale, represented by k_0, the vertical scale σ, the slope of the surface spectrum α, and the directional distribution $\tilde{\mathcal{D}}(\beta)$] on the acoustic Doppler spectra are discussed, based on the numerical predictions obtained by means of the Kirchhoff model. Flow condition 3 was chosen as the baseline for the numerical simulations, because in this condition the characteristic horizontal and vertical scales of the rough surface were smaller. As a result, the relation between the surface spectrum and the acoustic Doppler spectrum is straightforward[8] and the results are more easily interpreted. The effects on the acoustic spectra of larger characteristic scales, which are representative of different flow conditions, are illustrated in Fig. 5, and discussed toward the end of this section.

The effects of the choice of the surface directional distribution $\tilde{\mathcal{D}}(\beta)$ and the surface spectrum slope α on the acoustic Doppler spectrum for the adopted source-receiver geometry are shown in Fig. 4. Figure 4 compares the simulated Doppler spectra obtained from the synthetic realizations of a surface with the mean surface velocity $U_0 = 0.30$ m/s and characteristic scales $k_0 = 120.8$ rad/m and $\sigma = 0.25$ mm measured in condition 3, but with different choices of $\tilde{\mathcal{D}}(\beta)$ and α. In Figs. 4–9, the spectra are shown in dB relative to the power of the signal reflected by a flat surface.

Figure 4 shows two simulations obtained with the Poisson directional surface distribution and $\alpha = 5$ and $\alpha = 7$, and one simulation obtained with the sech^2 distribution with $\alpha = 5$. The predicted Doppler spectra display a sharp peak at the Doppler frequency equal to 0 and with the amplitude slightly smaller than 0 dB, which is independent on α and $\tilde{\mathcal{D}}(\beta)$. This peak was caused by the coherent reflection at the specular point.[11] The Doppler spectra decay smoothly and rapidly with the frequency at both the positive and negative Doppler frequencies. Surface waves with the same direction of propagation can cause both positive and negative Doppler shifts depending on the region where scattering occurs. With the acoustic setup used for this study, where the source is located downstream with respect to the receiver, the surface waves that propagate downstream would yield a positive Doppler frequency shift if scattering occurred only in the region nearer to the receiver where $x < 0$. Conversely, the same waves would yield a negative Doppler shift if scattering occurred only in the region nearer to the source where $x > 0$. Waves that propagate upstream would yield a positive Doppler shift if scattering occurred only in the region where $x > 0$, and a negative Doppler shift if scattering occurred only where $x < 0$. With the setup adopted in this study, both regions with $x < 0$ and $x > 0$ were responsible for scattering. Therefore, the Doppler spectra at both positive and negative frequencies were affected by surface waves that propagated in all directions. The asymmetry of the Doppler spectra was due to the asymmetry of the projected directivity pattern of the transducer on the surface.

Due to the small vertical scale of the surface fluctuations compared to the acoustic wavelength in condition 3, there is a direct relationship between the simulated Doppler spectra shown in Fig. 4 and the spectrum of the rough surface at the same frequency.[8] As a consequence, the directional distribution and the slope of the surface spectrum affect the Doppler spectra in different frequency ranges. The Doppler spectra in Fig. 4 show an increase of the decay rate when the absolute value of the Doppler frequency is larger than $2k_0U_0 = 72.5$ rad/s. This frequency marks the separation between the region of the acoustic spectrum that is governed by the directional distribution $\tilde{\mathcal{D}}(\beta)$ and the region that is governed by the spectrum slope α. According to Eq. (18), the effect of the directional distribution used in the numerical simulations was essentially limited to the free surface waves with the wavenumber modulus equal to k_0, and with the frequency smaller or equal to $2k_0U_0$. In this frequency range, a larger average absolute difference of

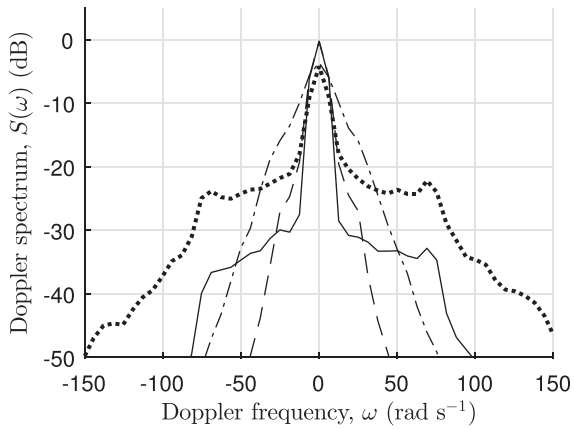

FIG. 5. Examples of the simulated Doppler spectra for $U_0 = 0.30$ m/s, Poisson distribution, $\alpha = 5$. (Solid) $k_0 = 120.8$ rad/m, $\sigma = 0.25$ mm, (dashed) $k_0 = 27.1$ rad/m, $\sigma = 0.25$ mm, (dotted) $k_0 = 120.8$ rad/m, $\sigma = 1$ mm, (dashed-dotted) $k_0 = 27.1$ rad/m, $\sigma = 1$ mm.

2.3 dB in the acoustic Doppler spectra was found between the two simulations with the same α and different directional distribution. The average difference in the acoustic Doppler spectra between the two simulations with the Poisson distribution and different α was only 0.6 dB. In contrast, the slope of the spectrum α affected the waves with the wavenumber larger than k_0 and the frequency larger than $2k_0U_0$. Accordingly, at the absolute Doppler frequencies larger than $2k_0U_0$, the two simulations with the same α and different directional distribution differed by less than 4 dB up to a Doppler frequency of 750 rad/s, while the Doppler spectrum obtained with $\alpha = 7$ decreased faster with the Doppler frequency. The difference from the similar simulation obtained with $\alpha = 5$ was 0.9 dB at the frequency $2k_0U_0$, and became as large as 19 dB at 750 rad/s.

The effects of the characteristic surface scales k_0 and σ on the predicted Doppler spectra is illustrated in Fig. 5 for a set of surface realizations obtained with $\alpha = 5$ and with the Poisson distribution, moving with the mean surface velocity $U_0 = 0.30$ m/s. With respect to the baseline condition 3 with $k_0 = 120.8$ rad/m and $\sigma = 0.25$ mm, a reduction of the characteristic wavenumber k_0 from 120.8 rad/m to 27.1 rad/m caused a narrowing of the Doppler spectrum, with little effect on its amplitude. Instead, the increase of the standard deviation of the surface elevation σ from 0.25 mm to 1 mm caused the increase of the Doppler spectrum away from the central peak at zero Doppler frequency, and a 4 dB reduction of the amplitude of this peak with respect to the baseline simulation. This behavior can be explained by the loss of coherence of the reflected signal when the amplitude of the surface waves becomes comparable with the acoustic wavelength.[11] When both the horizontal and vertical characteristic surface scales are increased (dashed-dotted line in Fig. 5), the width of the central peak is governed by the standard deviation of the surface elevation, σ, and by the transducer-receiver arrangement.[11]

V. EXPERIMENTAL RESULTS

A. Comparison between the numerical and experimental results

A comparison between the numerical predictions of the Doppler spectra and their experimental measurements, obtained for flow condition 3, is shown in Fig. 6. The measured Doppler spectrum in Fig. 6 compares to the numerical results presented in Figs. 4 and 5 for small σ and large k_0. The sharp peak at zero Doppler frequency, the asymmetry, and the increase of the rate of decay of the Doppler spectrum at the absolute Doppler frequency larger than $2k_0U_0$ can all be observed in Fig. 6. The predictions of the Doppler spectrum obtained with the numerical model and shown in Fig. 4 are presented again in Fig. 6. The model overestimated the amplitude of the measured Doppler spectrum at the Doppler frequencies of $-2k_0U_0$ and $2k_0U_0$ by approximately 12 dB and 7 dB, respectively. This large deviation is explained by the larger amplitude of the frequency spectrum of the synthetic surface at the frequency of $2k_0U_0$, discussed in Sec. III C. Below this frequency, the difference between the measurement and the simulations with the Poisson distribution was found to be 2.8 dB in average. The sech^2 distribution had a larger average error of 3.8 dB. Therefore, only the results obtained with the Poisson distribution are presented in the rest of this paper.

A distinction must be made for the behavior at larger positive and negative frequencies. At positive Doppler frequencies higher than $2k_0U_0$, both simulations with $\alpha = 5$ and $\alpha = 7$ and the Poisson distribution initially approximate the measurements with a maximum error of less than 4 dB. The simulated spectrum obtained with $\alpha = 7$ decreased more rapidly, and underestimated the measurements by 8 dB at the Doppler frequency of 200 rad/s. At the same frequency, the difference between the measurements and the simulation with $\alpha = 5$ was 1 dB. At even higher frequencies, the difference increased as the measured spectrum became essentially flat. This could have been a consequence of measurement noise or a manifestation of second-order effects.[31] In the negative frequency range, the measured spectrum appeared to decay more rapidly compared to the numerical results. In the range between -200 rad/s and $-2k_0U_0 = -72.5$ rad/s, the average difference between the measured and predicted spectra was 7.7 dB for the simulation with $\alpha = 5$ and 3.9 dB for the simulation with $\alpha = 7$. Based on the acoustic setup used for this study, where the incident acoustic waves propagated predominantly toward the negative x-direction, and assuming that most surface waves propagated downstream toward the positive x-direction, the negative frequency range was related mainly to the reflections from the region closer to the transducer than to the microphone. In this region the directivity varied more rapidly, and its representation in terms of Eq. (1) was believed to be less reliable. Therefore, the model with the Poisson distribution and $\alpha = 5$ was considered to provide a better approximation to the measured Doppler spectrum in condition 3.

The behavior of the acoustic Doppler spectrum shown in Fig. 6 for condition 3 was observed consistently across the other tested flow conditions. Changes of the flow Froude number and the characteristic surface scales were found to also affect the spectra, as already illustrated in Fig. 5. Figures 7 and 8 show the comparisons between the measured and modeled Doppler spectra obtained for flow conditions 6 and 9, respectively. These conditions were representative of the intermediate and larger Froude numbers across the tested

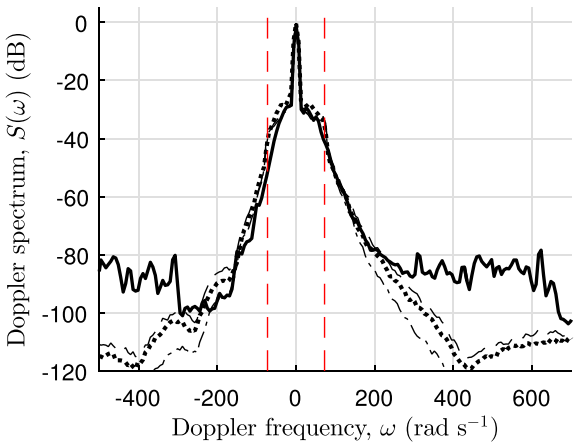

FIG. 6. (Color online) Examples of the measured and simulated Doppler spectra for flow condition 3. (Solid) Measured, (dashed) simulated, $\alpha = 5$, Poisson distribution, (dashed-dotted) simulated, $\alpha = 7$, Poisson distribution, (dotted) simulated, $\alpha = 5$, sech^2 distribution. (Red lines) $\omega = \pm 2k_0U_0$.

range of conditions. The most noticeable difference between the experimental results for these conditions and those for condition 3 is the behavior of the peak at the zero Doppler frequency. The amplitude of this peak decreased progressively from condition 3 (Fig. 6) to condition 6 (Fig. 7) and condition 9 (Fig. 8). As the amplitude of the peak decreased, its width apparently increased. As a result, for condition 9 the acoustic Doppler spectrum decayed smoothly from zero Doppler frequency, as shown in Fig. 8. This behavior was similar to the one observed in Fig. 5 for the synthetic surface realizations with small k_0 and a relatively large characteristic surface elevation $\sigma = 1$ mm. According to Table I, comparable characteristic horizontal and vertical scales of the surface were found in conditions 6 and 9, where $k_0 = 47.0$ rad/m, $\sigma = 1.21$ mm, and $k_0 = 27.1$ rad/m, $\sigma = 2.03$ mm, respectively.

In Figs. 7 and 8, the change of slope of the measured Doppler spectra at the Doppler frequency of $2k_0U_0$ is less visible than in Fig. 6. For conditions 6 and 9, the larger relative amplitude of the surface waves meant that the relation between the Doppler spectra and the surface spectra was not as straightforward as for condition 3. The average difference between the simulations and the measurements in the region where the absolute frequency is less than $2k_0U_0$ was found to be 2.2 dB and 2.0 dB for conditions 6 and 9, respectively. A larger difference of ~5 dB was found at the frequency of $2k_0U_0$, where the model still predicted a small peak of the Doppler spectra. This likely represents a limitation of the surface model, which predicts sharper knees of the surface spectrum, as discussed in Sec. III C.

At higher positive Doppler frequencies, the difference between the measured spectrum and the model for condition 6 reduced to less than 2 dB, before increasing again at a frequency of ~140 rad/s. Above this frequency, the measured spectrum shown in Fig. 7 decayed considerably less rapidly than that predicted by both models. A similar behavior was observed at the negative frequencies, although here the error began to increase later at −175 rad/s. Figure 8 shows a similar behavior for condition 9, although in this case the range where the model with $\alpha = 5$ was accurate within 2 dB was limited to the absolute Doppler frequencies below 90 rad/s. Although a direct comparison between the frequency of the

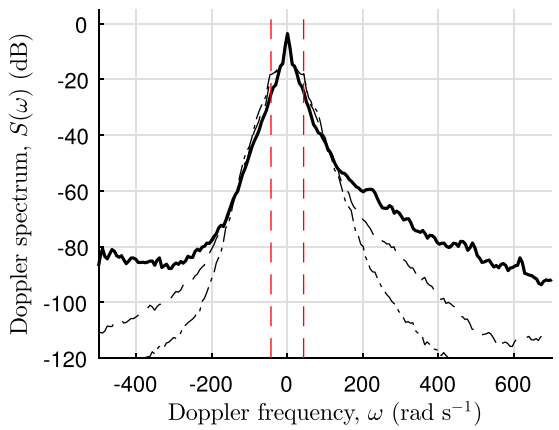

FIG. 7. (Color online) Examples of the measured and simulated Doppler spectra for flow condition 6. (Solid) Measured, (dashed) simulated, $\alpha = 5$, (dashed-dotted) simulated, $\alpha = 7$. (Red lines) $\omega = \pm 2k_0U_0$.

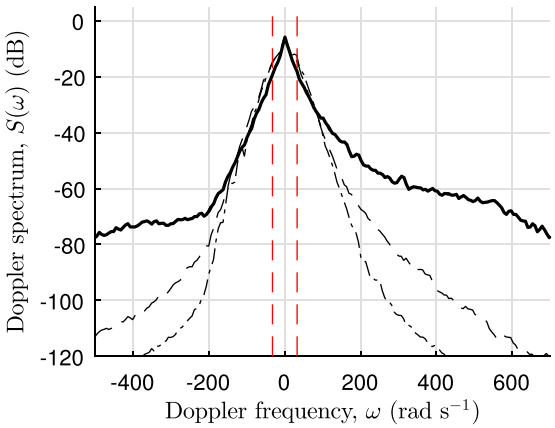

FIG. 8. (Color online) Examples of the measured and simulated Doppler spectra for flow condition 9. (Solid) Measured, (dashed) simulated, $\alpha = 5$, (dashed-dotted) simulated, $\alpha = 7$. (Red lines) $\omega = \pm 2k_0U_0$.

surface waves and the Doppler frequencies may not be possible when the amplitude of the surface waves is large, it is suggested that the larger amplitude of the Doppler spectra at high absolute Doppler frequencies may indicate a larger amplitude of shorter and faster waves on the surface compared to what is predicted by the power-function surface spectrum used for the simulations. In fact, the comparison between the predicted acoustic Doppler spectra obtained with $\alpha = 5$ and $\alpha = 7$ and shown in Figs. 4 and 5 suggests that a decrease of the slope of the surface spectrum causes an increase of the amplitude of the Doppler spectra at high Doppler frequencies. The constraints imposed by the Kirchhoff approximation did not allow performing simulations with smaller slopes of the surface spectrum, especially at the shorter scales. This impeded the matching of the predictions with the model over the whole range of frequencies. A two-scale model[32] could be more appropriate for investigating the behavior of the Doppler spectra at the higher frequencies, which could also be affected by the nonlinear dynamics of short surface waves.[4]

In this study, the comparison between the numerical simulations and the measurements at lower Doppler frequencies demonstrates that the acoustic Doppler spectra are influenced by the spectra of the free surface roughness, and the proposed surface model and the acoustic model based on the Kirchhoff approximation provide an adequate representation of the surface dynamics and of its effects on the scattering of airborne ultrasound at low and moderate Doppler frequencies.

B. Variation of the Doppler spectra with the flow condition

In Sec. V A the link between the acoustic Doppler spectra and the surface roughness spectra was observed for flow conditions 3, 6, and 9. Now, it is of interest to verify if a similar link can be found over a wider range of flow conditions. The Doppler spectra measured in all flow conditions reported in Table I are shown in Figs. 9(a)–9(c). Figure 9(a) displays the results obtained for flow conditions 1, 2, and 3, which had the lower Froude numbers, smaller than 0.49. Figure 9(b) shows the Doppler spectra measured in

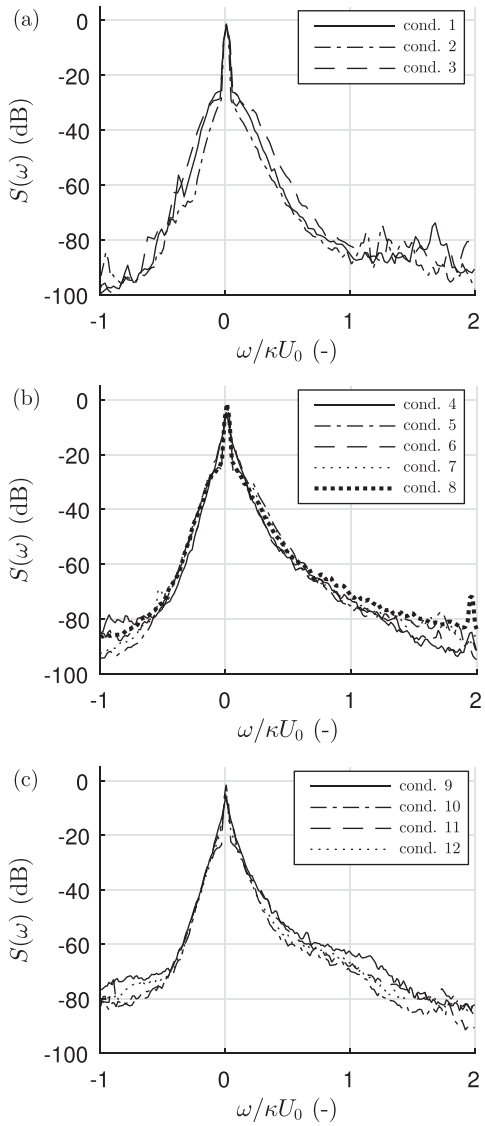

FIG. 9. Measured Doppler spectra plotted against the non-dimensional frequency $\omega/\kappa U_0$. All flow conditions.

conditions 4–8, with the intermediate Froude numbers between 0.49 and 0.61. Figure 9(c) displays the results obtained in conditions 9–12, with the larger Froude numbers, larger than 0.61.

In Fig. 9, the frequency has been non-dimensionalized based on the characteristic frequency κU_0, where κ is the acoustic wavenumber and U_0 is the flow mean surface velocity. Dolcetti *et al.*[15] have shown that the frequency spectra of the surface elevation scale consistently across a wide range of flow conditions when plotted against the non-dimensional frequency ω/k_0U_0. Due to the observed link between the surface spectra and the Doppler spectra, it would appear natural to employ the same non-dimensionalization for the Doppler spectra of Fig. 9. When this was attempted, the average maximum difference between all Doppler spectra in each range of Froude numbers was found to be between 8 and 15 dB. This was calculated as the average across all frequencies of the difference between the largest and the smallest Doppler spectra, in the range where the spectral amplitude was larger than −70 dB. In comparison, the same difference evaluated for the spectra without non-dimensionalization was 4.3, 7.5, and 8.4 dB, for the low, intermediate, and higher Froude number ranges, respectively. The proposed non-dimensionalization based on κU_0 led to a more consistent behavior of the spectra at the intermediate and higher Froude numbers. In this case, all spectra within the intermediate and high Froude numbers groups were found to be included in a narrow amplitude band with the average width of 5.0 dB and 4.4 dB, respectively. A much less consistent behavior was found in the lower Froude number range with the same non-dimensionalization, where the average maximum difference among the three conditions 1–3 was found to be 10 dB, higher than when the spectra were represented against the dimensional frequency. In spite of this larger difference, the behavior of the Doppler spectra for conditions 1 and 2 shown in Fig. 9(a) was more similar to that of condition 3 than it was to that of the remaining flow conditions, as the spectra did not show the longer tail at higher frequencies, which can be observed in Figs. 9(b) and 9(c). In general, the flow conditions 1–3, 4–8, and 9–12 showed a behavior similar to that of conditions 3, 6, and 9 (Figs. 6, 7, and 8, respectively), which have been discussed in Sec. V A.

The fact that the Doppler spectra behave similarly when the frequency is non-dimensionalized based on the quantity κU_0 suggests an apparent linear dependence of the Doppler shifts on the flow velocity. This is of notice since it potentially allows estimating the mean surface velocity U_0 remotely from the measurement of the Doppler spectra of scattered ultrasound signals. Although limited at the present stage by a partial understanding of the effects of the Froude number on the dynamics of the free surface roughness, the measurement of the flow velocity based on forward scattered Doppler would be advantageous compared to similar techniques based on backscattering. In fact, the signal-to-noise ratio is significantly larger in forward scattering than in backscattering, and a better understanding of the surface behavior at the larger scales allows an easier interpretation of the measurements. This was demonstrated by a close fit between the measured acoustic Doppler spectra and those predicted with the numerical model, as shown in Figs. 6–8.

Additional information about the water surface can be extracted from the observation of the measured spectra in Fig. 9. The sharp peak at zero Doppler frequency can be observed clearly in conditions 1, 2, 3, 5, 7, 8, and 11. In these conditions, the Doppler spectra also decay more rapidly above a frequency that has been previously identified with the characteristic frequency $2k_0U_0$. This frequency is related to the mean depth and the mean surface velocity of the flow through Eq. (4). In the remaining conditions 4, 6, 9, 10, and 12, the Doppler spectrum decays smoothly from zero Doppler frequency, for the reasons discussed in Sec. IV. These are the flow conditions where the standard deviation of the surface elevation, σ, was larger than 1 mm, or 12.7% of the acoustic wavelength, and where the characteristic horizontal scale represented by the wavenumber k_0 was larger. These results demonstrate the direct link between the measured Doppler spectra and the spatial horizontal and vertical scales of the water surface elevation.

It should be noted that, across all conditions investigated in this study, the surface waves had an amplitude smaller

than the ultrasound wavelength, although still larger than prescribed by a small perturbation method. Similar conditions can be found in real rivers, at low flow velocities and large depths (e.g., Ref. 29), although larger surface waves may occur in fast, energetic flows. The model presented here is believed to remain valid when relatively larger waves are considered, as long as the Kirchhoff approximation is satisfied, although in this case the behavior of the acoustic Doppler spectra may differ from the one that is observed in Fig. 9. Additional investigations are needed in order to characterize the behavior of the Doppler spectra over a wider range of flow conditions.

VI. CONCLUSIONS

The measurements of the Doppler power spectra of the signals of ultrasound forward scattered by the dynamic free surface of a turbulent open channel water flow have been presented and compared with the predictions obtained with a Kirchhoff approximation combined with a linear random-phase model of the dynamic rough water surface. Across the tested range of flow conditions, the results show the existence of a link between the acoustic Doppler spectra and the characteristic spatial and dynamic scales of the water surface fluctuations. When the characteristic spatial scales of the surface elevation are relatively small, the Doppler spectra display a change of slope at the characteristic frequency of the dynamically rough surface, equal to twice the product of the flow mean surface velocity and the wavenumber of the stationary waves. Larger characteristic scales of the surface can be clearly recognized since they cause the smoothing of the central peak of the Doppler spectra at the zero Doppler frequency.

Across all the tested flow conditions, the Doppler spectra have been found to scale consistently with the mean surface velocity of the flow. It has been suggested that this scaling may be used for the remote measurement of the velocity in an open channel flow. The flow Froude number was also found affecting the acoustic Doppler spectra at the higher Doppler frequencies. The Doppler spectra of forward scattered signals are governed by the larger and dominant scales of the water surface. The dynamic behavior of these waves has been well characterized in previous studies of the free surface of turbulent flows over rough beds.[15] As a result, the behavior of the Doppler spectra measured for this type of flow can be modeled and predicted accurately based on a simple surface model. The forward scattering Doppler spectra are characterized by a much larger signal-to-noise ratio compared to the more traditional backscattering Doppler spectra, which are affected by the dynamics of short and poorly understood waves on the free surface. It is suggested that the analysis of the Doppler spectra of ultrasound signals forward scattered by the water surface can provide a robust technique for the remote characterization of the flow conditions in turbulent open channel flows such as small rivers and open channels.

ACKNOWLEDGMENTS

The authors are grateful to Nigel Smith for his technical support with setting up the experiments, Professor Kirill V. Horoshenkov for his helpful comments on this manuscript, and two anonymous reviewers for their useful comments. This work was supported by the Engineering and Physical Sciences Research Council, UK (EPSRC) Grant No. EP/N029437/1.

APPENDIX

The Poisson directional distribution and the sech^2 directional distribution are defined as[25]

$$\tilde{\mathcal{D}}(\beta) = \frac{1}{2\pi}\frac{(1-b^2)}{\left[1-2b\cos(\beta-\pi)+b^2\right]} \tag{A1}$$

and

$$\tilde{\mathcal{D}}(\beta) = \frac{1}{\tan(b\pi)}\frac{b}{2\cosh^2(b(\beta-\pi))}, \tag{A2}$$

respectively. The condition $\tilde{\mathcal{D}}(\pi)/\tilde{\mathcal{D}}(0) = 10^{1.5}$, which was inspired by the observation in Ref. 15, yields $b = 0.698$ for the Poisson distribution, $b = 0.768$ for the sech^2 distribution.

The form of the directional spectrum presented in Eq. (18) allows splitting the cosine series of Eq. (14) into three distinct sums: one for the waves with constant wavenumber $k_p = k_0$ and variable $\beta_q = q\Delta\beta$, and two for the waves with variable wavenumber $k_p = p\Delta k \geq k_0$ and constant $\beta_q = 0$ or $\beta_q = \pi$. For each of these waves, the coefficients a_{pq} were calculated by integrating the delta functions analytically over k or β, and then approximating the remaining integral with a midpoint rule. As a result, a random realization of the free surface elevation function ζ at the time t was expressed by

$$\begin{aligned}\zeta(x,y,t) = &\sum_{q=1}^{2\pi/\Delta\beta} B_q\xi_{pq}\cos\left[k_0\cos(\beta_q)x + k_0\sin(\beta_q)y\right.\\ &\left.-\Omega(k_0,\beta_q)t+\Phi_{pq}\right]_{p=k_0/\Delta k} + \sum_{p=k_0/\Delta k}^{k_N/\Delta k} C_p\xi_{pq}\\ &\times\cos\left[k_p x-\Omega(k_p,0)t+\Phi_{pq}\right]_{q=0} + \sum_{p=k_0/\Delta k}^{k_N/\Delta k} C_{-p}\xi_{pq}\\ &\times\cos\left[-k_p x-\Omega(k_p,\pi)t+\Phi_{pq}\right]_{q=\pi/\Delta\beta},\end{aligned} \tag{A3}$$

where k_N is the wavenumber of the shortest simulated waves, and the coefficients of the three series were calculated as

$$\begin{aligned}\frac{B_q^2}{2} &= \Psi_0\tilde{\mathcal{D}}(\beta)k_0\Delta\beta\\ &\approx\int_{\Delta k_p}\int_{\Delta\beta_q}\tilde{\Psi}(k)\tilde{\mathcal{D}}(\beta)\delta(k-k_0)k\,dk\,d\beta,\end{aligned} \tag{A4}$$

$$\begin{aligned}\frac{C_p^2}{2} &= \Psi_0\left(\frac{k_p}{k_0}\right)^{-\alpha}\tilde{\mathcal{D}}(0)\Delta k\\ &\approx\int_{\Delta k_p}\int_{\Delta\beta_q}\tilde{\Psi}(k)\tilde{\mathcal{D}}(\beta)H(k-k_0)\delta(\beta)\,dk\,d\beta,\end{aligned} \tag{A5}$$

and

$$\frac{C_{-p}^2}{2} = \mathcal{L}\frac{C_p^2}{2}. \tag{A6}$$

It should be noted that the sums over p in Eq. (A3) were limited to $k_0/\Delta k \le p \le k_N/\Delta k$, so that only the waves with $k_0 \le k_p \le k_N$ have been modeled. The constant Ψ_0 was found by imposing

$$\sum_q \frac{B_q^2}{2} + \sum_p \frac{C_p^2 + C_{-p}^2}{2} = \int_0^\infty \int_0^{2\pi} \Psi(k,\beta) k\, dk\, d\beta = \sigma^2, \tag{A7}$$

which yields

$$\Psi_0 = \frac{\sigma^2}{k_0}\left[1 + \frac{(1+\mathcal{L})}{\alpha - 1}\tilde{\mathcal{D}}(0)\right]^{-1}. \tag{A8}$$

The ratio of the energy localized at the wavenumber k_0 relative to the energy of the whole spectrum is equal to $k_0\Psi_0/\sigma^2$, and it can be calculated based on the directional distribution and the spectrum slope α from Eq. (A8). Based on the Poisson distribution, this quantity is 81% with $\alpha = 5$ and 87% with $\alpha = 7$, which shows how these waves contribute to most of the energy. Even larger values of 91% and 94%, are predicted based on the sech^2 distribution.

[1]D. E. Barrick, "The ocean waveheight nondirectional spectrum from inversion of the HF sea-echo Doppler spectrum," Remote Sens. Environ. **6**, 201–227 (1977).
[2]D. E. Barrick, "Extraction of wave parameters from measured HF radar sea-echo Doppler spectra," Radio Sci. **12**, 415–424, https://doi.org/10.1029/RS012i003p00415 (1977).
[3]D. E. Barrick, "First-order theory and analysis of MF/HF/VHF scatter from the sea," IEEE Trans. Antenn. Propag. **20**, 2–10 (1972).
[4]W. C. Keller, W. J. Plant, R. A. Petitt, and E. A. Terray, "Microwave backscatter from the sea: Modulation of received power and Doppler bandwidth by long waves," J. Geophys. Res.-Oceans **99**, 9751–9766, https://doi.org/10.1029/94JC00082 (1994).
[5]J. T. Johnson, J. V. Toporkov, and G. S. Brown, "A numerical study of backscattering from time-evolving sea surfaces: Comparison of hydrodynamic models," IEEE Trans. Geosci. Remote Sens. **39**, 2411–2420 (2001).
[6]W. J. Plant, W. C. Keller, and K. Hayes, "Measurement of river surface currents with coherent microwave systems," IEEE Trans. Geosci. Remote Sens. **43**, 1242–1257 (2005).
[7]J. E. Costa, R. T. Cheng, F. P. Haeni, N. Melcher, K. R. Spicer, E. Hayes, W. J. Plant, K. Hayes, C. C. Teague, and D. E. Barrick, "Use of radars to monitor stream discharge by noncontact methods," Water Resour. Res. **42**, W07422, https://doi.org/10.1029/2005WR004430 (2006).
[8]C. C. Teague, "Bistatic-radar techniques for observing long-wavelength directional ocean-wave spectra," IEEE Trans. Geosci. Electron. **9**, 211–215 (1971).
[9]J. Zhang and E. W. Gill, "Extraction of ocean wave spectra from simulated noisy bistatic high-frequency radar data," IEEE J. Ocean. Eng. **31**, 779–796 (2006).
[10]W. Huang, E. W. Gill, W. Xiongbin, and L. Li, "Measurement of sea surface wind direction using bistatic high-frequency radar," IEEE Trans. Geosci. Remote Sens. **50**, 4117–4122 (2012).
[11]B. E. Parkins, "Scattering from the time-varying surface of the ocean," J. Acoust. Soc. Am. **42**, 1262–1267 (1967).
[12]S. Grosdidier, P. Forget, Y. Barbin, and C. A. Guérin, "HF bistatic ocean Doppler spectra: Simulation versus experimentation," IEEE Trans. Geosci. Remote Sens. **52**, 2138–2148 (2014).
[13]C. C. Teague, D. E. Barrick, P. M. Lilleboe, and R. T. Cheng, "Canal and river tests of a RiverSonde streamflow measurement system," in *Proceedings of the International Geoscience and Remote Sensing Symposium 2001, IGARSS'01*, Sydney, Australia (July 9–13, 2001), Vol. 3, pp. 1288–1290.
[14]C. C. Teague, D. E. Barrick, and P. M. Lilleboe, "Geometries for streamflow measurement using a UHF RiverSonde," in *Proceedings of the International Geoscience and Remote Sensing Symposium 2003, IGARSS'03*, Toulouse, France (July 21–25, 2003), Vol. 7, pp. 4286–4288.
[15]G. Dolcetti, K. V. Horoshenkov, A. Krynkin, and S. J. Tait, "Frequency-wavenumber spectrum of the free surface of shallow turbulent flows over a rough boundary," Phys. Fluids **28**, 105105 (2016).
[16]M. S. Longuet-Higgins, "The statistical analysis of a random, moving surface," Philos. Trans. R. Soc. A **249**, 321–387 (1957).
[17]K. V. Horoshenkov, A. Nichols, S. J. Tait, and G. A. Maximov, "The pattern of surface waves in a shallow free surface flow," J. Geophys. Res.-Earth **118**, 1864–1876, https://doi.org/10.1002/jgrf.20117 (2013).
[18]G. Dolcetti, "Remote monitoring of shallow turbulent flows based on the Doppler spectra of airborne ultrasound," Ph.D. dissertation, The University of Sheffield, Sheffield, UK, 2017, Chap. 5.
[19]A. Krynkin, G. Dolcetti, and S. Hunting, "Acoustic imaging in application to reconstruction of rough rigid surface with airborne ultrasound waves," Rev. Sci. Instrum. **88**, 024901 (2017).
[20]P. M. Morse and K. U. Ingard, *Theoretical Acoustics* (Princeton University Press, Princeton, NJ, 1968), p. 381.
[21]J. C. Burns, "Long waves in running water," Math. Proc. Cambridge **49**, 695–706 (1953).
[22]J. D. Fenton, "Some results for surface gravity waves on shear flows," IMA J. Appl. Math. **12**, 1–20 (1976).
[23]F. G. Bass and I. M. Fuks, *Wave Scattering from Statistically Rough Surfaces, in International Series in Natural Philosophy* (Oxford Pergamon, Oxford, UK, 1979), Vol. 93, p. 225.
[24]J. V. Toporkov and G. S. Brown, "Numerical simulations of scattering from time-varying, randomly rough surfaces," IEEE Trans. Geosci. Remote Sens. **38**, 1616–1625 (2000).
[25]H. E. Krogstad, "The directional wave spectrum," in *COST Action 714, Measuring and Analysing the Directional Spectra of Ocean Waves*, edited by D. Hauser, K. K. Kahma, H. E. Krogstad, S. Lehner, J. Monbaliu, and L. R. Wyatt (Office for Official Publications of the European Communities, Luxembourg, 2005), p. 45.
[26]S. A. Kitaigordskii, V. P. Krasitskii, and M. M. Zaslavskii, "On Phillips' theory of equilibrium range in the spectra of wind-generated gravity waves," J. Phys. Oceanogr. **5**, 410–420 (1975).
[27]R. Savelsberg and W. Van De Water, "Experiments on free-surface turbulence," J. Fluid Mech. **619**, 95–125 (2009).
[28]M. A. C. Teixeira and S. E. Belcher, "On the initiation of surface waves by turbulent shear flow," Dynam. Atmos. Oceans **41**, 1–27 (2006).
[29]C. J. Legleiter, C. D. Mobley, and B. T. Overstreet, "A framework for modeling connections between hydraulics, water surface roughness, and surface reflectance in open channel flows," J. Geophys. Res.-Earth **122**, 1715–1741, https://doi.org/10.1002/2017JF004323 (2017).
[30]S. N. Chandler-Wilde, "The boundary element method in outdoor noise propagation," Proc. Inst. Acoust. **19**, 27–50 (1997).
[31]K. Hasselmann, "Determination of ocean wave spectra from Doppler radio return from the sea surface," Nat. Phys. Sci. **229**, 16–17 (1971).
[32]G. R. Valenzuela, "Scattering of electromagnetic waves from a tilted slightly rough surface," Radio Sci. **3**, 1057–1066, https://doi.org/10.1002/rds19683111057 (1968).